American Mineralogist, Volume 96, pages 1593–1605, 2011

Static disorders of atoms and experimental determination of Debye temperature in pyrope: Low- and high-temperature single-crystal X-ray diffraction study

Akihiko Nakatsuka,[1,*] Mami Shimokawa,[1] Noriaki Nakayama,[1] Osamu Ohtaka,[2] Hiroshi Arima,[3] Maki Okube,[4] and Akira Yoshiasa[5]

[1]Graduate School of Science and Engineering, Yamaguchi University, Ube 755-8611, Japan
[2]Graduate School of Science, Osaka University, Toyonaka 560-0043, Japan
[3]J-PARC Center, Japan Atomic Energy Agency, Ibaraki 319-1195, Japan
[4]Materials and Structures Laboratory, Tokyo Institute of Technology, Yokohama 226-8503, Japan
[5]Graduate School of Science and Technology, Kumamoto University, Kumamoto 860-8555, Japan

Abstract

Low- and high-temperature single-crystal X-ray diffraction studies of synthetic pyrope garnet have been conducted at 20 temperature-points over a wide temperature range from 96.7 to 972.9 K. From precise structure refinements, the possibility of static disorder and anharmonic thermal vibration of Mg in the dodecahedral site, which has long been under debate, has been assessed together with the thermal expansion behavior. Application of the Debye model to the temperature dependence of the resulting mean square displacements (MSDs) of atoms shows that they clearly include significant static disorder components in all the constituent atoms, of which Mg has the most dominant static disorder component. The residual electron density analyses and the structure refinements based on the split-atom model at a low temperature of 96.7 K provide direct proof of the Mg static disorder. Anharmonic structure refinements applying the Gram-Charlier expansion up to the fourth-rank tensor show that the anharmonic contribution to atomic thermal vibrations begins to appear in all atoms except Si at a high temperature of $T > 800$ K. However, at lower temperatures, anharmonic refinements show no sign of anharmonic thermal vibrations on any atom and instead provide an indication of their static disorder.

Keywords: Garnet, static disorder, Debye temperature, anharmonic thermal vibration, thermal expansion, single-crystal X-ray diffraction

Introduction

Garnets have attracted much attention in various research fields from solid-state physics to Earth science. Since silicate garnets are major constituents of the Earth's crust, upper mantle, and transition zone, they are important to elucidate physical properties, phase relations, and dynamics in the Earth's interior. Although most natural garnets occur commonly as complex multi-component solid solutions, the most significant component in garnets of mantle origin is pyrope ($Mg_3Al_2Si_3O_{12}$), composed of the major elemental components of the mantle. Therefore, the investigation of the structural, physical, and thermodynamic properties of pyrope is important for the understanding of the Earth's mantle.

Pyrope crystallizes in cubic symmetry with the highest space group $Ia\bar{3}d$. The cubic garnets $X_3Y_2Z_3O_{12}$ have three symmetrically distinct cation sites (Fig. 1): the eightfold-coordinated X site [Wyckoff position 24*c* at (0.125, 0, 0.25)], the sixfold-coordinated Y site [Wyckoff position 16*a* at (0, 0, 0)], and the fourfold-coordinated Z site [Wyckoff position 24*d* at (0.375, 0, 0.25)]. The X, Y, and Z cations are coordinated dodecahedrally, octahedrally, and tetrahedrally by O atoms, located at the Wyckoff position 96*h* at (x, y, z), respectively. These three types of coordination polyhedra link in a complex manner; a ZO_4 tetrahedron shares edges with two XO_8 dodecahedra, a YO_6 octahedron with six XO_8 dodecahedra, and a XO_8 dodecahedron with two ZO_4 tetrahedra, four YO_6 octahedra, and four other XO_8 dodecahedra. The linkage between tetrahedra and octahedra is made by mutually sharing all corners. In pyrope, which is stable only at high pressure as confirmed by geological occurrence and synthetic experiments, the dodecahedral, octahedral, and tetrahedral sites are occupied by Mg, Al, and Si, respectively. In terms of crystal chemistry, this coordination environment of Mg is apparently unreasonable because the dodecahedral cavity size is too large for the ionic radius of Mg, which would fit better into the octahedral site as expected from Pauling's first rule (Pauling 1929). This geometric anomaly implies the possibility of positional disorder (static disorder) or large thermal vibration (dynamic disorder) of Mg (including the possibility of anharmonic contribution to the thermal vibration). Indeed, structural and thermodynamic studies of pyrope have reported the following experimental observations suggesting these possibilities: (1) anomalously large atomic displacement parameters (ADPs) of Mg in pyrope observed by diffraction method (Gibbs and Smith 1965; Novak and Gibbs 1971; Armbruster et al. 1992; Pavese et al. 1995; Artioli et al. 1997); (2) an anomalously high heat capacity at low temperature observed in pyrope (Haselton and Westrum 1980; Kieffer 1980; Hofmeister and Chopelas 1991) and a positive excess entropy observed in its solid solutions with

* E-mail: tuka@yamaguchi-u.ac.jp

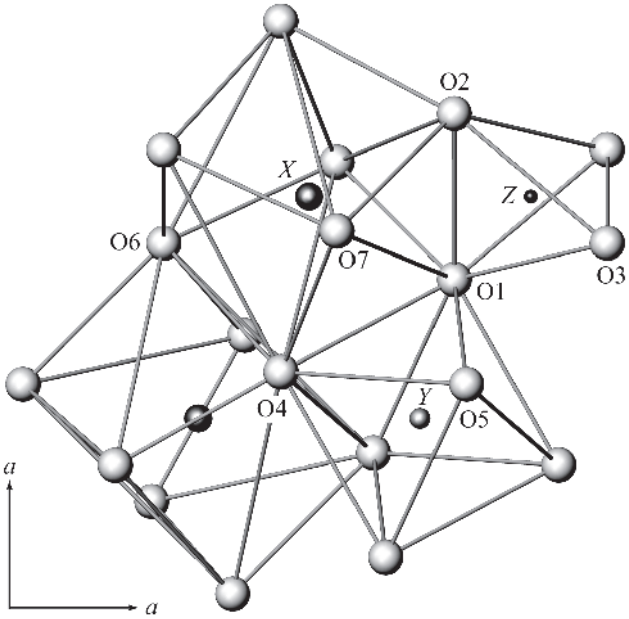

FIGURE 1. Section of the garnet structure.

Mg-rich compositions (Cressey 1981). To date, there have been considerable debates as to whether these observations originate in the static nature (Zemann 1962; Cressey 1981; Hofmeister and Chopelas 1991; Pilati et al. 1996) or the dynamic nature (Gibbs and Smith 1965; Armbruster et al. 1992; Geiger et al. 1992b; Sawada 1993; Pavese et al. 1995; Artioli et al. 1997; Kolesov and Geiger 1998; Winkler et al. 2000) of the Mg disorder.

A direct method to confirm static disorder is to observe a splitting of electron density maxima around disordered atoms, but it is often difficult to detect a small degree of site-splitting by this method. Indeed, the previous attempt on pyrope resulted in failure (Meagher 1975). Another available method is to extract contribution of static disorder to ADPs, including both effects of static disorder and dynamic disorder, from their temperature dependence. According to the Debye model, the ADPs, corresponding to MSDs of atoms, show approximately linear temperature dependence above the Debye temperature (Willis and Pryor 1975). Accordingly, the existence of a positive 0 K intercept of the linear extrapolation of high-temperature ADP values has been frequently cited as evidence for static disorder in various materials. To our knowledge, only two studies have employed this approach for pyrope: a single-crystal X-ray diffraction study (Pavese et al. 1995) on a synthetic pyrope in the range of 30–973 K, and a single-crystal neutron diffraction study (Artioli et al. 1997) on a natural pyrope with a composition of $(Mg_{0.92}Fe_{0.05}Ca_{0.03})Al_2Si_3O_{12}$ in the range of 30–1173 K. The former study failed to find evidence of the Mg static disorder because of a large uncertainty of the extrapolated values to 0 K. The latter study showed that the extrapolated values to 0 K were significantly positive in Mg and O atoms, but concluded that this was unlikely to be due to static disorders of both atoms because the low-temperature structure refinements based on possible split-atom models for these atoms failed to improve the reliability indices. The discussions in both studies were based on a limited number of ADP data, although a lot more data points in the high-temperature range are necessary for reliable extrapolations. In addition, their extrapolations were performed including data down to much lower temperatures than the reported Debye temperature of pyrope (698 K; Suzuki and Anderson 1983); the static disorder components obtained by this way could therefore include some zero-point energy contributions.

These two diffraction studies also examined anharmonicity of atomic thermal vibration by applying the Gram-Charlier expansion up to the fourth-rank tensor to the Debye-Waller factors of Mg atom only (Pavese et al. 1995) or all atoms (Artioli et al. 1997). Both studies reported that some of the refined third- and fourth-rank tensor coefficients of Mg atom (Pavese et al. 1995) or both Mg and O atoms (Artioli et al. 1997) became slightly significant above 700 K and hence asserted that anharmonic contribution to their thermal vibrations appeared above this temperature. However, they could detect no sign of anharmonicity at room temperature and below, where the anomalously high heat capacity was observed, confirming a previous report on a natural pyrope with nearly end-member composition at room temperature (Sawada 1993). Thus, all the structural investigations have not yet provided any evidence for a static disorder or anharmonic thermal vibration at low temperature of Mg, and only suggested large anisotropy of the Mg displacement (Zemann 1962; Gibbs and Smith 1965; Novak and Gibbs 1971; Meagher 1975; Armbruster et al. 1992; Geiger et al. 1992b; Sawada 1993; Pavese et al. 1995; Artioli et al. 1997; Kolesov and Geiger 1998).

The displacement behavior of Mg in pyrope has also been discussed based on theoretical approaches (Winkler et al. 1991, 2000; Pilati et al. 1996). Lattice-dynamic calculations showed that the calculated ADPs of Mg in pyrope and Fe in almandine ($Fe_3Al_2Si_3O_{12}$) are much smaller than their experimental values and argued that a model based on static disorder can best explain this anomalous discrepancy (Pilati et al. 1996). However, there are also claims based on density functional theory calculations that this anomalous feature of Mg in pyrope can be due to anharmonicity of its thermal vibration (Winkler et al. 2000).

Thus, atomic displacement behavior of Mg in pyrope is still a controversial issue. ADPs are quite sensitive to the correlation with other variable parameters. All possible corrections for the effects affecting diffraction intensities are necessary for their reliable determination. Since the effect of thermal diffuse scattering (TDS) on the diffraction intensities becomes more conspicuous at high temperatures owing to the increase in atomic thermal vibrations, this effect, which has hitherto been ignored in pyrope, should be corrected. Also, the use of natural samples should be avoided for the investigation of atomic displacement behavior although they were used in several of previous diffraction studies on pyrope (Sawada 1993; Artioli et al. 1997). This is because the presence of impurity atoms in the Mg site inevitably leads to static disorders, which masks the static disorder of Mg.

In the present study, we conduct precise structure analyses of a synthetic pyrope at 20 temperature-points in the range of 96.7–972.9 K using single-crystal X-ray diffraction. To determine the Debye temperature and distinguish between static and dynamic disorders of atoms, we investigate temperature dependence of MSDs on the basis of the Debye model including a static disorder component. In addition, the electron density distribution around the Mg site at low temperature is examined in detail to confirm the existence of a static disorder of Mg. Contributions

of anharmonicity to atomic thermal vibrations and the thermal expansion are also discussed.

EXPERIMENTS AND ANALYSIS

Single-crystal growth under high pressure

Single crystals of pyrope ($Mg_3Al_2Si_3O_{12}$) were grown at high pressure and high temperature (5 GPa, 1573 K) under the presence of a small amount of PbO flux, using a 700-ton cubic anvil type high-pressure apparatus. A 12.5 mm cube of pyrophyllite was used as a pressure-transmitting medium. Special grade reagents (99.99%) of MgO, Al_2O_3, and SiO_2 were used as starting materials, and mixed in the molar ratio $MgO:Al_2O_3:SiO_2 = 3:1:3$ together with 10 mol% of PbO flux. The mixtures were enclosed in a platinum capsule and then put into a MgO capsule, after which it was inserted into a cylindrical carbon heater embedded in the pyrophyllite cube; the MgO capsule was used as an insulator between the platinum capsule and the carbon heater. After being kept under the desired condition (5 GPa, 1573 K) for 2.5 h, the sample was gradually cooled to 1273 K at 0.7 K/min and then quenched by shutting off the electric power supply. The pressure was slowly released and the sample was recovered at ambient conditions. Numerous 100–200 μm big single crystals of pyrope were found in the recovered sample. EPMA analyses could detect no contamination of grown crystals by the PbO flux, and the crystal compositions showed no deviation from the ideal cation-ratio of Mg:Al:Si = 3:2:3.

Intensity measurements and structure refinements

A single crystal with a size of $0.14 \times 0.11 \times 0.11$ mm^3 was selected for X-ray diffraction intensity measurements and was put into a silica-glass capillary. Intensity data were collected at 20 temperature-points in the range of 96.7–972.9 K using a Rigaku AFC-7R four-circle diffractometer with graphite-monochromatized Mo*K*α radiation (λ = 0.71069 Å) at the operating condition of 50 kV and 200 mA. Data collections below room temperature were conducted by directly cooling the crystal through a continuous cold N_2 gas flow generated using a Rigaku GN2 low-temperature apparatus. For data collections above room temperature, high temperature was achieved by a continuous flow of N_2 gas heated by an electric resistance heater. Prior to data collections, sample temperatures were calibrated using a K-type thermocouple placed exactly at the sample position. Temperature fluctuation during the data collections was kept within ±0.2 K. The unit-cell parameters at each temperature were determined by the least-squares method from a set of 25 reflections within the range of $44° \le 2\theta \le 51°$. Intensity data of reflections were collected within $2° \le 2\theta \le 100°$ for each temperature using the continuous ω–2θ scan mode. Between 1967 and 2023 reflections were measured for each temperature. The intensity data were corrected for Lorentz-polarization factors, absorption effects (ψ-scan method), and TDS effects. The TDS correction was based on a model of first-order scattering due to one-phonon process of acoustic mode. The elastic constants (C_{11}, C_{12}, C_{44}) at each investigated temperature used for TDS correction were estimated from the linear interpolation based on their temperature derivatives determined by Sinogeikin and Bass (2002). After these corrections, the intensity data were averaged in Laue symmetry $m\bar{3}m$ to give between 663 and 678 independent reflections for each temperature point. Of these, independent reflections with $|F_o| \le 6\sigma(|F_o|)$ were eliminated. Even if independent reflections had intensities of $|F_o| > 6\sigma(|F_o|)$ after averaging, those averaged from data set of equivalent reflections including reflection(s) with $|F_o| \le 6\sigma(|F_o|)$ were also discarded since these reflections were potentially affected by multiple scattering as has been reported in pyrope (Armbruster et al. 1992). Moreover, as in the previous studies (Pavese et al. 1995; Gramaccioli et al. 2002), independent reflections with $(\sin\theta)/\lambda < 0.24$ Å^{-1} were eliminated to reduce secondary extinction effects and to avoid dependence on atomic charge as far as possible in the choice of atomic scattering factors. In all the present structure refinements, only nine independent reflections were eliminated by this cutoff criterion for low-angle reflections. It is notable, thereby, that the reliability indices (R = 0.0147–0.0181, wR = 0.0071–0.0104 for each temperature; Table 1) were remarkably improved in comparison with those from the refinements without this cutoff criterion (R = 0.0214–0.0265, wR = 0.0133–0.0162 for each temperature). Moreover, as shown in Figure 2, the equivalent isotropic ADPs (U_{eq}) of Mg and O atoms from the refinements without the cutoff criterion are significantly larger than those from the refinements with the cutoff criterion although the U_{eq} values of Al and Si atoms show almost no difference between both refinements. This is an indication of the extinction effect on intensities of low-angle reflections, showing the validity of our refinement strategy. Finally, between 211 and 328 independent reflections were used in the present refinements at each temperature point. Internal residuals of the equivalent reflections (R_{int}) varied between 0.0085 and 0.0130 for each temperature.

The structure refinements were carried out by minimizing the function $\Sigma w(|F_o|-|F_c|)^2$ using a full matrix least-squares program RADY (Sasaki 1987). Scattering factors of Mg^{2+}, Al^{3+}, Si^{4+} (*International Tables for Crystallography*, Table 6.1.1.3; Wilson 1992), and O^{2-} (Tokonami 1965) were used. Anomalous dispersion coefficients for each scattering factor were taken from *International Tables for Crystallography* (Table 4.2.6.8; Wilson 1992). Several correction models for the secondary extinction effects were attempted during the refinements, and the isotropic correction of Type I (Becker and Coppens 1974a, 1974b) with a Lorentzian mosaic spread distribution model yielded the best fits. After the refinements based on the harmonic displacement model, the Gram-Charlier expansion up to the fourth-rank tensor, expressed by Equation 1, was applied to the Debye-Waller factor $T(h)$ in order to assess the anharmonicity of atomic thermal vibrations:

$$T(h) = \left(1 + \frac{(2\pi i)^3}{3!}\gamma_{ijk}h_ih_jh_k + \frac{(2\pi i)^4}{4!}\delta_{ijkl}h_ih_jh_kh_l\right)\exp\left(-\beta_{ij}h_ih_j\right) \quad (1)$$

where β_{ij}, γ_{ijk}, and δ_{ijkl} are the second-, third-, and fourth-rank tensor coefficients, respectively, and h stands for the Miller indices for a given reflection. In the harmonic refinements, the anharmonic components, i.e., the tensor coefficients higher than the second-rank, are ignored. The structure refinements at each temperature converged smoothly to R = 0.0147–0.0181 and wR = 0.0071–0.0104 for the harmonic model and to R = 0.0108–0.0147 and wR = 0.0051–0.0082 for the anharmonic model. The summary of data collection and refinement parameters is given in Table 1, and their full details are deposited in Supplementary Table S1 of the supplementary materials[1]. The positional parameters and equivalent isotropic ADPs (U_{eq}) from the harmonic refinements are given in Table 2, and the anisotropic ADPs (β_{ij}) are deposited in Supplementary Table S2[1]. The structural parameters from the anharmonic refinements are deposited in Supplementary Table S3[1]. CIF[1] is available on deposit.

RESULTS AND DISCUSSION

Thermal expansion

Unit-cell volume. The temperature dependence of the unit-cell volumes is shown in Figure 3. The data were fitted to the following equation (Suzuki et al. 1979) derived from the Grüneisen theory of volumetric thermal expansion, using a non-linear weighted least-squares method:

$$V(T) = \frac{V_t}{2k_0a_v}\left(1 + 2k_0 - \sqrt{1 - \frac{4k_0U}{Q_0}}\right) \quad (2)$$

$$U = 9nRT\left(\frac{T}{\Theta_D}\right)^3\int_0^{\frac{\Theta_D}{T}}\frac{x^3}{\exp(x)-1}dx$$

where $Q_0 = K_0V_0/\gamma_G$, $k_0 = (dK_0/dP - 1)/2$, and $a_v = V_t/V_0$; V_0 and K_0 are the volume and the bulk modulus at 0 K, respectively, and V_t is the volume at a reference temperature t; γ_G is the Grüneisen parameter, U the internal energy, n the number of atoms in the formula unit, R the gas constant, Θ_D the Debye temperature, and T the absolute temperature. The data above 200 K, well represented by Equation 2, were employed in this fit. The fitting parameters resulted in values of $\Theta_D = 717(20)$ K, $Q_0 = 16.54(10) \times 10^6$ J/mol, and $a_v(=V_{295}/V_0) = 1.00339(8)$, by fixing k_0 to 1.50 reported for a natural pyrope (Suzuki and Anderson 1983). These resulting

[1] Deposit item AM-11-050, Supplementary Tables 1–3, CIF. Deposit items are available two ways: For a paper copy contact the Business Office of the Mineralogical Society of America (see inside front cover of recent issue) for price information. For an electronic copy visit the MSA web site at http://www.minsocam.org, go to the *American Mineralogist* Contents, find the table of contents for the specific volume/issue wanted, and then click on the deposit link there.

TABLE 1. Summary of data collection and refinement parameters

T (K)	96.7	122.3	173.7	223.3	273.6
Crystal data and data collection					
Cell setting	Cubic	Cubic	Cubic	Cubic	Cubic
Space group	$Ia\bar{3}d$	$Ia\bar{3}d$	$Ia\bar{3}d$	$Ia\bar{3}d$	$Ia\bar{3}d$
a (Å)	11.4401(3)	11.4425(3)	11.4450(3)	11.4508(2)	11.4548(2)
V (Å^3)	1497.25(7)	1498.16(7)	1499.15(7)	1501.45(5)	1503.01(5)
No. of measured reflections	1967	1967	1967	1973	1973
No. of independent reflections	663	663	663	663	663
No. of observed reflections [$F_o > 6\sigma(F_o)$]	330	333	329	335	337
R_{int}	0.0104	0.0108	0.0098	0.0098	0.0088
$2\theta_{max}$ (°)	100	100	100	100	100
Refinement on harmonic model					
R	0.0151	0.0154	0.0159	0.0153	0.0155
wR	0.0084	0.0104	0.0094	0.0089	0.0081
S	1.66	2.02	1.82	1.69	1.63
No. of reflections	321	324	320	326	328
No. of parameters	18	18	18	18	18
Refinement on anharmonic model					
R	0.0131	0.0138	0.0136	0.0130	0.0133
wR	0.0066	0.0082	0.0073	0.0069	0.0063
S	1.41	1.72	1.53	1.41	1.37
No. of reflections	321	324	320	326	328
No. of parameters	62	62	62	62	62

T (K)	295	322.8	373.5	423.3	472.6
Crystal data and data collection					
Cell setting	Cubic	Cubic	Cubic	Cubic	Cubic
Space group	$Ia\bar{3}d$	$Ia\bar{3}d$	$Ia\bar{3}d$	$Ia\bar{3}d$	$Ia\bar{3}d$
a (Å)	11.4572(3)	11.4592(2)	11.4641(3)	11.4690(4)	11.4730(4)
V (Å^3)	1503.94(7)	1504.74(5)	1506.67(7)	1508.63(9)	1510.18(9)
No. of measured reflections	1973	1973	1973	1974	1982
No. of independent reflections	665	665	665	665	665
No. of observed reflections [$F_o > 6\sigma(F_o)$]	326	335	333	293	282
R_{int}	0.0088	0.0113	0.0085	0.0122	0.0123
$2\theta_{max}$ (°)	100	100	100	100	100
Refinement on harmonic model					
R	0.0147	0.0164	0.0149	0.0181	0.0179
wR	0.0086	0.0089	0.0082	0.0104	0.0094
S	1.65	1.76	1.64	2.17	2.00
No. of reflections	317	326	324	284	273
No. of parameters	18	18	18	18	18
Refinement on anharmonic model					
R	0.0131	0.0139	0.0127	0.0147	0.0131
wR	0.0067	0.0067	0.0064	0.0080	0.0065
S	1.38	1.45	1.37	1.84	1.52
No. of reflections	317	326	324	284	273
No. of parameters	62	62	62	62	62

TABLE 1. —*CONTINUED*

T (K)	523.0	572.9	622.9	672.9	723.0
Crystal data and data collection					
Cell setting	Cubic	Cubic	Cubic	Cubic	Cubic
Space group	$Ia\bar{3}d$	$Ia\bar{3}d$	$Ia\bar{3}d$	$Ia\bar{3}d$	$Ia\bar{3}d$
a (Å)	11.4801(4)	11.4848(3)	11.4893(3)	11.4960(3)	11.5023(4)
V (Å^3)	1513.01(9)	1514.87(7)	1516.62(7)	1519.30(7)	1521.78(9)
No. of measured reflections	1982	1982	2008	2008	2008
No. of independent reflections	667	667	667	676	676
No. of observed reflections [$F_o > 6\sigma(F_o)$]	304	301	297	280	270
R_{int}	0.0093	0.0092	0.0086	0.0088	0.0097
$2\theta_{max}$ (°)	100	100	100	100	100
Refinement on harmonic model					
R	0.0151	0.0166	0.0149	0.0153	0.0154
wR	0.0076	0.0082	0.0080	0.0082	0.0077
S	1.53	1.66	1.59	1.66	1.56
No. of reflections	295	292	288	271	261
No. of parameters	18	18	18	18	18
Refinement on anharmonic model					
R	0.0127	0.0129	0.0134	0.0141	0.0125
wR	0.0060	0.0058	0.0061	0.0063	0.0057
S	1.31	1.28	1.34	1.41	1.28
No. of reflections	295	292	288	271	261
No. of parameters	62	62	62	62	62

T (K)	773.1	823.1	873.1	922.9	972.9
Crystal data and data collection					
Cell setting	Cubic	Cubic	Cubic	Cubic	Cubic
Space group	$Ia\bar{3}d$	$Ia\bar{3}d$	$Ia\bar{3}d$	$Ia\bar{3}d$	$Ia\bar{3}d$
a (Å)	11.5078(6)	11.5136(4)	11.5195(4)	11.5244(6)	11.5291(5)
V (Å^3)	1523.96(14)	1526.29(9)	1528.63(9)	1530.56(14)	1532.44(12)
No. of measured reflections	2012	2014	2014	2014	2023
No. of independent reflections	676	678	678	678	678
No. of observed reflections [$F_o > 6\sigma(F_o)$]	262	254	254	240	220
R_{int}	0.0087	0.0130	0.0093	0.0086	0.0102
$2\theta_{max}$ (°)	100	100	100	100	100
Refinement on harmonic model					
R	0.0156	0.0165	0.0160	0.0148	0.0173
wR	0.0078	0.0096	0.0079	0.0071	0.0088
S	1.60	1.96	1.60	1.46	1.84
No. of reflections	253	245	245	231	211
No. of parameters	18	18	18	18	18
Refinement on anharmonic model					
R	0.0119	0.0143	0.0129	0.0108	0.0124
wR	0.0055	0.0075	0.0061	0.0051	0.0062
S	1.26	1.70	1.38	1.17	1.47
No. of reflections	253	245	245	231	211
No. of parameters	62	62	62	62	62

values agree very well with those reported for the natural pyrope [Θ_D = 698(16) K, Q_0 = 16.5(2) × 10^6 J/mol, a_v (=V_{298}/V_0) = 1.00337(4)] (Suzuki and Anderson 1983); in particular, the present Θ_D value of 717(20) K is also consistent with the Debye temperature of 779 K estimated from acoustic wave velocities at 300 K (Suzuki and Anderson 1983). The temperature dependence of the volumetric thermal expansion coefficients $\alpha_V(T)$ [=1/$V(T)$·$dV(T)/dT$] determined from numerical differentiation of $V(T)$ is also given in Figure 3. The $\alpha_V(T)$ increases steeply with heating up to about 350 K, after which it increases almost linearly with a gentle slope above about 700 K.

Interatomic distances. Figures 4 and 5 show the temperature dependence of the interatomic distances normalized at their values at 96.7 K and their thermal expansion coefficients $\alpha_L(T)$ [=1/$L(T)$·$dL(T)/dT$], respectively, where $L(T)$ is interatomic distances as a function of temperature and functions obtained from the parabolic fits were employed for $L(T)$. The $\alpha_L(T)$ was fitted to the approximation $\alpha_L(T) = a_0 + a_1T + a_2T^{-2}$ ($a_2 \leq 0$) (Fei 1995), and the coefficients a_0, a_1, and a_2 determined for each interatomic distance are tabulated in Table 3. For comparison with the previous studies, the conventional mean thermal expansion coefficients $<\alpha_L>$ [=1/L(295)·$\Delta L/\Delta T$] are also listed in Table 3, where the slopes determined by the linear fits were employed for $\Delta L/\Delta T$. The present $<\alpha_L>$ values agree essentially with the reported ones (Meagher 1975; Pavese et al. 1995) (Table 3). On the other hand, as shown in Figure 5, the present $\alpha_L(T)$ values

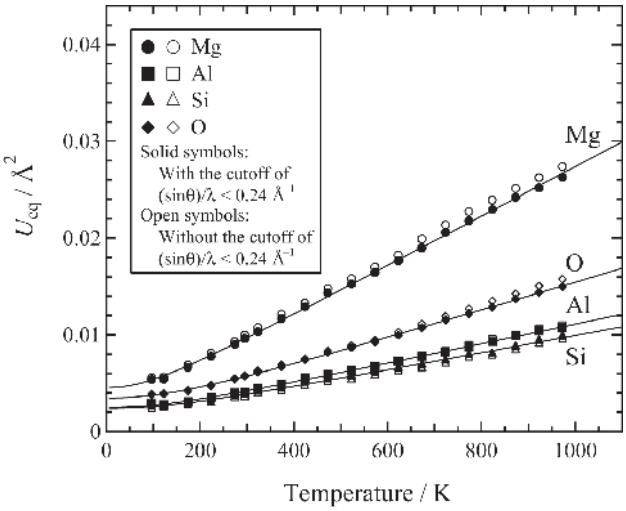

FIGURE 2. Temperature dependence of U_{eq}.

TABLE 2. Positional parameters and U_{eq} (Å²) from the harmonic refinements on the 24*c* model

T (K)	96.7	122.3	173.7	223.3	273.6
x (O)	−0.03290(4)	−0.03294(5)	−0.03298(5)	−0.03303(4)	−0.03295(4)
y (O)	0.05061(4)	0.05040(5)	0.05053(5)	0.05037(4)	0.05044(4)
z (O)	0.15333(4)	0.15337(5)	0.15350(5)	0.15341(4)	0.15340(4)
U_{eq} (Mg)	0.00539(1)	0.00540(3)	0.00662(3)	0.00777(3)	0.00901(3)
U_{eq} (Al)	0.00293(1)	0.00279(1)	0.00307(1)	0.00352(1)	0.00399(1)
U_{eq} (Si)	0.00258(1)	0.00267(1)	0.00293(1)	0.00317(1)	0.00372(1)
U_{eq} (O)	0.00384(3)	0.00388(3)	0.00422(3)	0.00472(3)	0.00540(3)
T (K)	295	322.8	373.5	423.3	472.6
x (O)	−0.03302(4)	−0.03301(4)	−0.03303(4)	−0.03309(6)	−0.03309(6)
y (O)	0.05020(4)	0.05015(5)	0.05010(4)	0.05018(6)	0.04999(6)
z (O)	0.15336(4)	0.15344(4)	0.15351(4)	0.15367(6)	0.15356(6)
U_{eq} (Mg)	0.00963(3)	0.01033(3)	0.01166(3)	0.01293(3)	0.01433(3)
U_{eq} (Al)	0.00410(1)	0.00443(1)	0.00484(1)	0.00553(1)	0.00591(1)
U_{eq} (Si)	0.00380(1)	0.00414(1)	0.00446(1)	0.00509(1)	0.00544(1)
U_{eq} (O)	0.00571(3)	0.00613(3)	0.00672(3)	0.00743(4)	0.00816(4)
T (K)	523.0	572.9	622.9	672.9	723.0
x (O)	−0.03313(4)	−0.03317(5)	−0.03317(5)	−0.03314(5)	−0.03323(5)
y (O)	0.04987(4)	0.04982(5)	0.04966(5)	0.04968(5)	0.04949(5)
z (O)	0.15345(4)	0.15357(5)	0.15359(5)	0.15356(5)	0.15357(5)
U_{eq} (Mg)	0.01527(3)	0.01644(3)	0.01767(3)	0.01898(3)	0.02058(3)
U_{eq} (Al)	0.00630(1)	0.00667(1)	0.00724(1)	0.00773(1)	0.00825(1)
U_{eq} (Si)	0.00568(1)	0.00614(1)	0.00652(1)	0.00689(1)	0.00735(1)
U_{eq} (O)	0.00868(3)	0.00926(3)	0.00998(3)	0.01072(4)	0.01153(4)
T (K)	773.1	823.1	873.1	922.9	972.9
x (O)	−0.03321(5)	−0.03330(6)	−0.03325(5)	−0.03328(5)	−0.03323(7)
y (O)	0.04947(5)	0.04901(6)	0.04934(5)	0.04926(5)	0.04926(7)
z (O)	0.15363(5)	0.15374(6)	0.15359(5)	0.15366(5)	0.15366(6)
U_{eq} (Mg)	0.02178(3)	0.02292(4)	0.02419(4)	0.02518(3)	0.02627(4)
U_{eq} (Al)	0.00879(1)	0.00932(1)	0.00990(1)	0.01042(1)	0.01077(1)
U_{eq} (Si)	0.00793(1)	0.00804(3)	0.00878(1)	0.00940(1)	0.00985(3)
U_{eq} (O)	0.01219(4)	0.01286(5)	0.01371(4)	0.01437(4)	0.01498(5)

Notes: Wyckoff positions: Mg, 24*c* at (0.125, 0, 0.25); Al, 16*a* at (0, 0, 0); Si, 24*d* at (0.375, 0, 0.25); O, 96*h* at (*x*, *y*, *z*).

show considerably different temperature dependence from the one reported by Pavese et al. (1995), obtained in the same way as in the present study, where the latter has much larger $d\alpha_L(T)/dT$ especially in the interatomic distances of the dodecahedron and octahedron. This overestimation in the previous result (Pavese et al. 1995) is likely due to large uncertainty for the parabolic fits of the interatomic distances made using only few data-points.

The $\alpha_L(T)$ values of Mg-O4 bond length, composed of Mg and O atoms forming the unshared dodecahedral edge, are

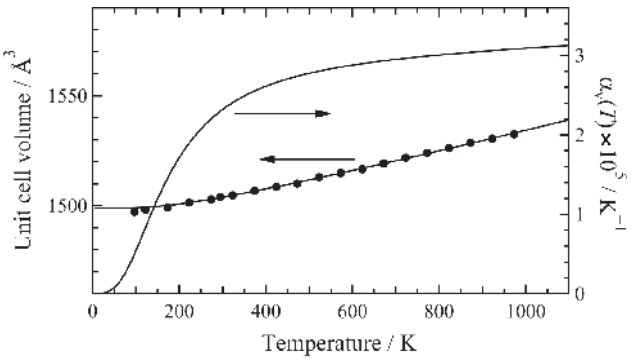

FIGURE 3. Temperature dependence of the unit-cell volume and the volumetric thermal expansion coefficient $\alpha_V(T)$. The volume data above 200 K were fitted to Equation 2.

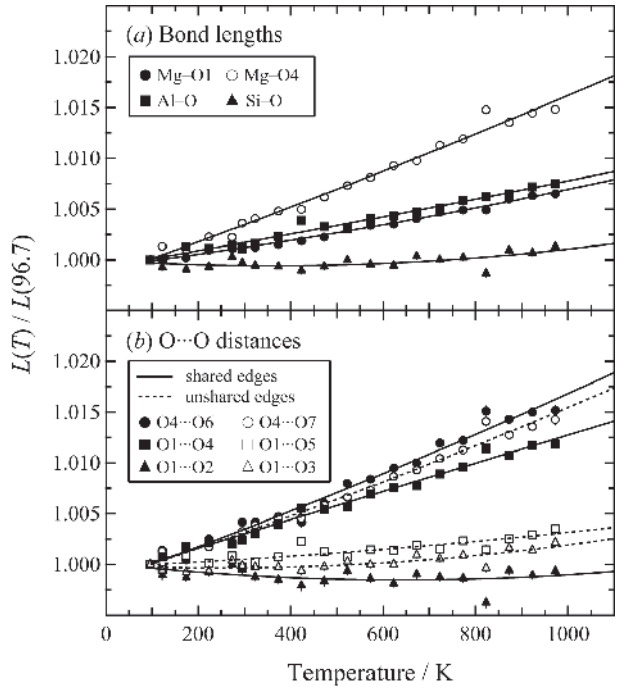

FIGURE 4. Temperature dependence of interatomic distances [$L(T)$] normalized to their values at 96.7 K [$L(96.7)$]: (**a**) bond lengths, (**b**) O···O distances.

consistently more than twice as large over the investigated temperature range as those of Mg-O1 bond length, composed of Mg and O atoms forming the dodecahedral-tetrahedral shared edge (Fig. 5a). The $<\alpha_L>$ values of both bonds are consistent with the reported ones (Meagher 1975; Pavese et al. 1995) (Table 3). The larger expansion of *X*-O4 bond lengths is also observed in many other garnets, such as almandine ($Fe_3Al_2Si_3O_{12}$) (Armbruster et al. 1992; Geiger et al. 1992a), spessartine ($Mn_3Al_2Si_3O_{12}$) (Geiger and Armbruster 1997; Rodehorst et al. 2002), andradite ($Ca_3Fe_2Si_3O_{12}$) (Armbruster and Geiger 1993), and grossular ($Ca_3Al_2Si_3O_{12}$) (Meagher 1975; Geiger and Armbruster 1997; Rodehorst et al. 2002). Due to geometric constraints of the garnet structure, *X*-O1 bond lengths are forced to be shorter than *X*-O4 bond lengths, despite the presence of adjacent tetrahedral cations across the dodecahedral-tetrahedral shared edges. This is to avoid

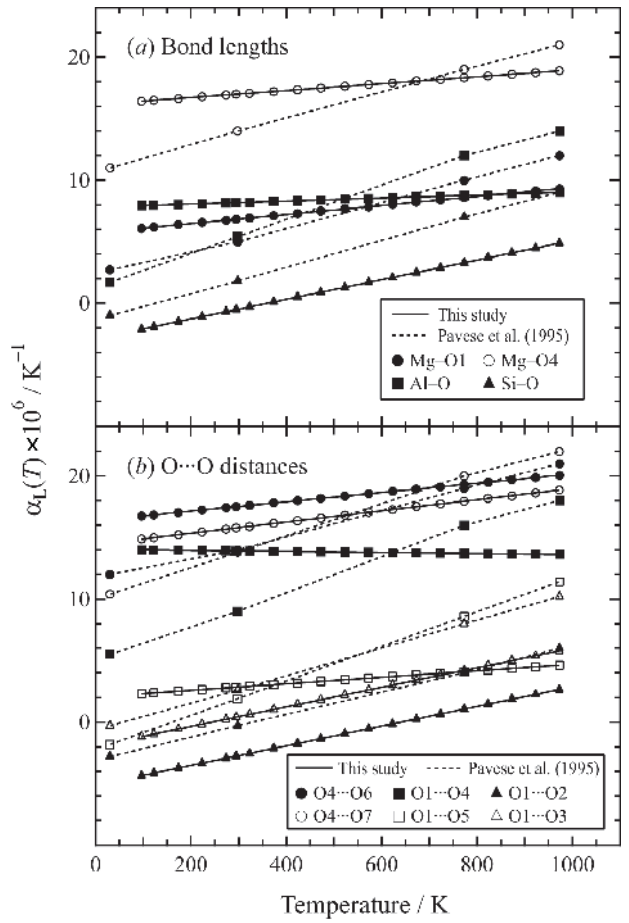

FIGURE 5. Temperature dependence of thermal expansion coefficients $\alpha_L(T)$ of (**a**) bond lengths and (**b**) O···O distances.

TABLE 3. Temperature-dependent thermal expansion coefficients $\alpha_L(T)$ (K^{-1}) of interatomic distances expressed by the polynomial approximation and their mean thermal expansion coefficients $<\alpha_L>$ (K^{-1})

	$\alpha_L(T) = a_0 + a_1T + a_2T^{-2}$ ($a_2 \le 0$)			$<\alpha_L> \times 10^6$		
	$a_0 \times 10^6$	$a_1 \times 10^9$	$a_2 \times 10^4$	This study	Pavese et al. (1995)	Meagher (1975)*
Mg-O1	5.7447	3.6708	−1.0132	7.7(2)	8.7(3)	7(3)
Mg-O4	16.1627	2.8024	−1.8734	17.7(5)	17.5(3)	19.0(6)
<Mg-O>	11.1121	3.2465	−1.5361	12.9(3)	13.1(3)	14(1)
Al-O	7.8183	1.2207	−0.3838	8.5(3)	9.6(3)	7.3(9)
Si-O	−2.8686	7.9713	−0.2637	1.3(5)	5.1(4)	1(2)
O4···O6	16.4005	3.7692	−2.6016	18.5(7)	17.7(4)	21(2)
O4···O7	14.4534	4.5284	−2.8263	16.9(5)	18.0(3)	18(5)
O1···O4	14.0491	−0.4300	0	13.9(4)	13.5(3)	13(2)
O1···O5	2.0548	2.6425	−0.3207	3.5(5)	6.1(2)	1(1)
O1···O2	−5.1144	7.9866	0	−0.9(7)	2.6(3)	−1(3)
O1···O3	−1.9363	7.9425	−0.5304	2.3(4)	6.1(3)	2 (3)

* Recalculated from the reported interatomic distances.

unreasonable lengths for *Y*-O bonds and unshared octahedral edges (Zemann 1962; Gibbs and Smith 1965). This geometric constraint leads stronger *X*-O1 bonds than *X*-O4 bonds, and consequently may control the smaller thermal expansion of Mg-O1 bond lengths in pyrope. As shown in Figure 5a, Mg-O1 bond lengths have slightly but significantly smaller thermal expansion coefficients than Al-O bond lengths up to 900 K, which confirms the previously reported relation of $<\alpha_L>$ values between both bonds (Meagher 1975; Pavese et al. 1995) (Table 3). However, this relation between both bonds is inverted above 900 K (Fig. 5a). The Si-O bond length does not vary largely with heating (Fig. 4a) and has much smaller thermal expansion coefficients than the remaining bond lengths (Fig. 5a and Table 3), over the investigated temperature range. This rigid SiO_4 tetrahedron has also been observed in other silicates, including garnets (Smyth and Hazen 1973; Brown and Prewitt 1973; Hazen and Finger 1982). However, it is noteworthy that the increase of $\alpha_L(T)$ in pyrope with heating is the largest for Si-O bond lengths (Fig. 5a).

In all polyhedra in pyrope, the shared edge lengths are shorter than the unshared ones, as predicted from Pauling's third rule (Pauling 1929). Shorter shared edges are commonly expected to expand more than longer unshared edges to avoid O···O repulsion. As shown in Figure 5b and Table 3, the dodecahedron and octahedron follow this prediction. On the other hand, the opposite situation is observed in the tetrahedron. This peculiar behavior of the tetrahedron can be explained by the presence of the strong cation-cation repulsion across the dodecahedral-tetrahedral shared edges, which we have discussed in various garnet compounds (Nakatsuka et al. 1995, 1999a, 1999b, 2003, 2004, 2005; Yoshiasa et al. 1997). To our knowledge, the $q_X \cdot q_Z / r^2_{X\text{-}Z}$ values, corresponding to the repulsion between dodecahedral and tetrahedral cations, of representative garnet compounds are in the ranges of 0.879–0.975 for silicate garnets (Novak and Gibbs 1971; Meagher 1975; Armbruster et al. 1992; Geiger et al. 1992a; Armbruster and Geiger 1993; Sawada 1993; Pavese et al. 1995; Pilati et al. 1996; Artioli et al. 1997; Geiger and Armbruster 1997; Rodehorst et al. 2002; Gramaccioli et al. 2002), 0.781–1.138 for germanate garnets (Levy and Barbier 1999), 0.916–1.016 for rare earth garnets (Euler and Bruce 1965; Nakatsuka et al. 1995, 1999a; Etschmann et al. 2001), and 0.503–0.867 for vanadate garnets (Lobanov et al. 1989; Nakatsuka et al. 2003, 2004; Tsirlin et al. 2007), where q_X and q_Z are valences of dodecahedral and tetrahedral cations, respectively, and $r_{X\text{-}Z}$ is distances between both cations. The $q_X \cdot q_Z / r^2_{X\text{-}Z}$ value of 0.975 in pyrope ranks among the largest of reported garnets; the presence of this strong Mg^{2+}-Si^{4+} repulsion is also evident from the displacement behaviors of both cations that will be discussed in the next section. Thus, the small expansion of the dodecahedral-tetrahedral shared edge compared to the unshared tetrahedral edge comes from the necessity to continuously shield this strong repulsion, leading to the increase in distortion of the tetrahedron at high temperatures in contrast to the dodecahedron and octahedron.

Temperature dependence of MSDs of atoms and their static disorders

The U_{eq} shown in Figure 2 corresponds to MSDs of atoms averaged over all directions. To examine the anisotropies of atomic displacements, we show in Figure 6 the temperature dependence of MSDs in the direction of the axis *j* (MSD_{axj}; *j* = 1, 2, 3), obtained from anisotropic ADPs, where the axis *j* represents the principal displacement-ellipsoid-axes for the cations and the crystal axes for O atom, principal the directions of the principal ellipsoid-axes vary with temperature (see Table 4 for their specific directions). The MSDs determined by diffraction method include the contributions of both static and dynamic disorders, and can be described on the basis of the Debye model as follows (Willis and Pryor 1975):

$$\mathrm{MSD} = \left\langle u^2 \right\rangle_{\mathrm{static}} + \left\langle u^2 \right\rangle_{\mathrm{dynamic}} = \left\langle u^2 \right\rangle_{\mathrm{static}} + \frac{3\hbar^2 T}{m k_{\mathrm{B}} \Theta_{\mathrm{D}}^2}\left[\Phi\left(\frac{\Theta_{\mathrm{D}}}{T}\right) + \frac{1}{4}\frac{\Theta_{\mathrm{D}}}{T}\right]$$
$$\Phi\left(\frac{\Theta_{\mathrm{D}}}{T}\right) = \frac{T}{\Theta_{\mathrm{D}}}\int_0^{\frac{\Theta_{\mathrm{D}}}{T}} \frac{x}{\exp(x)-1}\,dx \qquad (3)$$

where $\langle u^2 \rangle_{\mathrm{static}}$ is the temperature-independent static disorder component, $\langle u^2 \rangle_{\mathrm{dynamic}}$ the temperature-dependent dynamic disorder component, m the mass of atoms, k_{B} the Boltzmann constant, $\hbar$ the Planck constant, Θ_{D} the Debye temperature, and T the absolute temperature. This equation is strictly applicable only to isotropic atomic displacements in cubic monatomic solids (Willis and Pryor 1975), but application of this model to polyatomic solids has provided valuable insight even when applied to anisotropic displacement behaviors of their individual atoms (Wood et al. 2002; Christensen et al. 2006). The data of U_{eq} in Figure 2 and $\mathrm{MSD}_{\mathrm{ax}j}$ in Figure 6 were, therefore, fitted to Equation 3 using a non-linear least-squares method to determine the parameters $\langle u^2_{\mathrm{eq}} \rangle_{\mathrm{static}}$, $\langle u^2_{\mathrm{ax}j} \rangle_{\mathrm{static}}$, Θ_{Deq}, and $\Theta_{\mathrm{Dax}j}$; where $\langle u^2_{\mathrm{eq}} \rangle_{\mathrm{static}}$ and Θ_{Deq}, determined from the U_{eq} data, are the static disorder component and the Debye temperature averaged over all directions, respectively; $\langle u^2_{\mathrm{ax}j} \rangle_{\mathrm{static}}$ and $\Theta_{\mathrm{Dax}j}$, determined from the $\mathrm{MSD}_{\mathrm{ax}j}$ data, are the static disorder component and the Debye temperature in the direction of the axis j, respectively. The resulting values are provided in Table 4.

The temperature dependence of U_{eq} (Fig. 2) and $\mathrm{MSD}_{\mathrm{ax}j}$ (Fig. 6) is well represented by the Debye model over the investigated temperature range. Their variations are approximately linear in the high-temperature range and flatten below about 200 K. This behavior at low temperature is an obvious indication of the zero-point energy contribution. The resulting Θ_{Deq} values, corresponding to characteristic vibrational frequencies, become larger in order of Mg << Al < Si < O (Table 4). This relationship in the cations is reasonably consistent with bonding stiffness expected from the thermal expansion coefficients of the bond lengths. Also, the average of the Θ_{Deq} values [$=\{3\Theta_{\mathrm{Deq}}(\mathrm{Mg}) + 2\Theta_{\mathrm{Deq}}(\mathrm{Al}) + 3\Theta_{\mathrm{Deq}}(\mathrm{Si}) + 12\Theta_{\mathrm{Deq}}(\mathrm{O})\}/20$] is 731(1) K, being in excellent agreement with the Debye temperature of 717(20) K determined from the volumetric thermal expansion.

TABLE 4. Static disorder components (Å^2) and Debye temperatures (K) determined from the non-linear least-squares fits of MSDs to the Debye model

	Mg	Al	Si	O
$\langle u^2_{\mathrm{eq}} \rangle_{\mathrm{static}} \times 10^3$	1.43(10)	0.64(5)	0.68(6)	0.57(4)
Θ_{Deq}	482(2)	723(3)	754(4)	789(2)
$\langle u^2_{\mathrm{ax1}} \rangle_{\mathrm{static}} \times 10^3$	1.07(10)	0.65(13)	0.47(10)	0.43(8)
$\langle u^2_{\mathrm{ax2}} \rangle_{\mathrm{static}} \times 10^3$	1.09(23)	0.63(8)	0.79(7)	0.77(8)
$\langle u^2_{\mathrm{ax3}} \rangle_{\mathrm{static}} \times 10^3$	2.15(27)	0.63*	0.79*	0.54(9)
Θ_{Dax1}	638(4)	730(8)	787(8)	787(4)
Θ_{Dax2}	505(4)	720(5)	739(5)	719(3)
Θ_{Dax3}	391(2)	720†	739†	888(6)

Notes:
axis 1//[100], axis 2//[01$\bar{1}$], axis 3//[011] for Mg at (0.125, 0, 0.25).
axis 1//[111], axis 2⊥[111], axis 3⊥[111] for Al at (0, 0, 0).
axis 1//[100], axis 2⊥[100], axis 3⊥[100] for Si at (0.375, 0, 0.25).
axis 1//[100], axis 2//[010], axis 3//[001] for O at (*x*, *y*, *z*) in Table 2, where the directions of the axes 2 and 3 for Al and Si cannot be specified because of uniaxial ellipsoids.
* $\langle u^2_{\mathrm{ax3}} \rangle_{\mathrm{static}} = \langle u^2_{\mathrm{ax2}} \rangle_{\mathrm{static}}$.
† $\Theta_{\mathrm{Dax3}} = \Theta_{\mathrm{Dax2}}$.

The equivalent static-disorder components $\langle u^2_{\mathrm{eq}} \rangle_{\mathrm{static}}$ resulted in significantly positive values with the high reliability levels of 11–14σ for each atom (Table 4). The $\langle u^2_{\mathrm{eq}} \rangle_{\mathrm{static}}$ value of Mg is more than twice as large as those of the other atoms, which are nearly identical (≈0.0006 Å^2). Apart from the determination of the split Mg site (see below), the significant $\langle u^2_{\mathrm{eq}} \rangle_{\mathrm{static}}$ value of Mg is a strong indicator for the presence of static disorder on the Mg site. Since an O atom is bonded to two Mg, one Al, and one Si atoms, the Mg static disorder can cause some static disorder on the O position. The unexpected static disorders of Al and Si atoms, on the other hand, can be explained by the electrostatic repulsions of statically disordered (off-centered) Mg against Al across the dodecahedral-octahedral shared edge and against Si across the dodecahedral-tetrahedral shared edge. Consequently, the static disorders of Al and Si atoms can further increase the static disorder on the O position. The static disorders of Al, Si, and O atoms as expected from the significant $\langle u^2_{\mathrm{eq}} \rangle_{\mathrm{static}}$ values can thus be reasonably explained in terms of crystal chemistry. Lattice dynamic calculations (Pilati et al. 1996) have consistently shown a discrepancy between observed and calculated ADPs only for Mg. However, this is not in contradiction to the presence of the static disorder on the Al, Si, and O positions, because the degree of their static disorders is expected to be much smaller than that of Mg given the difference in the static disorder components between these atoms.

A closer examination of the anisotropy of atomic displacements can provide further insight into interatomic interactions. All anisotropic static-disorder components $\langle u^2_{\mathrm{ax}j} \rangle_{\mathrm{static}}$ show significantly positive values with reliability levels up to 11σ (Table 4). The temperature dependence of the anisotropic dynamic-disorder components $\langle u^2_{\mathrm{ax}j} \rangle_{\mathrm{dynamic}}$, given by $\mathrm{MSD}_{\mathrm{ax}j} - \langle u^2_{\mathrm{ax}j} \rangle_{\mathrm{static}}$, is shown in Figure 6. The dynamic disorder components of both Mg and Si atoms are the smallest in [100], corresponding to the direction of the Mg-Si vector, indicating the presence of strong repulsion between both cations across the dodecahedral-tetrahedral shared edge as has been discussed in our previous studies (Nakatsuka et al. 1995, 1999a, 1999b, 2003, 2004, 2005; Yoshiasa et al. 1997). Meanwhile, the dynamic disorder of Al is almost isotropic, indicating a much smaller interaction with adjacent Mg cations across the dodecahedral-octahedral shared edges. The same situation is also observed in the anisotropies of static disorder components ($\langle u^2_{\mathrm{ax}j} \rangle_{\mathrm{static}}$) of the cations (Table 4). It follows that the static disorders of Mg and Si atoms in combination with the anisotropies of their dynamic disorders help to avoid a structural instability caused by strong Mg-Si repulsion.

Split-atom site of Mg

When we consider the split-atom sites of Mg displaced from the averaged position (24*c* site), the following three cases are possible based on symmetry constraints: (1) a 48*f* site (x, 0, 0.25) displaced along [100] (48*f* model); (2) a 48*g* site (0.125, y, 0.25 – y) displaced along [01$\bar{1}$] (48*g* model); (3) a 96*h* site (x, y, z) slightly offset from the 24*c* site (96*h* model). On the basis of this prediction, we examined the residual electron density distribution around the 24*c* site at 96.7 K in detail, to directly observe the static disorder of Mg. Figure 7 shows the difference Fourier maps at 96.7 K after the anisotropic refinement on the 24*c* model (the normal model without any Mg static disorder).

No significant residual electron density peaks nearby the 24*c* site can be detected along [100] and [01$\bar{1}$], which correspond to the directions of the principal ellipsoid-axes of Mg with the smallest anisotropic static-disorder component (Table 4). Although these observations are likely to exclude the 48*f* and the 48*g* models from possible Mg static disorder models, we conducted structure refinements of these models and compared the results with that of the 24*c* model as a test. In the refinement assuming the 48*f* model, the Mg positional parameter, *x*, did not converge at all even in the isotropic displacement model. Meanwhile, the refinement assuming the 48*g* model successfully converged in the anisotropic displacement model, but the refined Mg positional parameter, *y* [=0.0005(7)], showed no significant deviation from the 24*c* site. In addition, the resulting *R*-values (R = 0.0150, wR = 0.0084) and U_{eq}(Mg) value [=0.00547(3) Å^2] showed no significant reduction from those in the anisotropic refinement on the 24*c* model [R = 0.0151, wR = 0.0084, U_{eq}(Mg) = 0.00539(1) Å^2]. Thus, these two models are not suitable for possible Mg static disorder models.

In contrast, residual electron density peaks with a height of 0.14 eÅ^{-3} were observed at equivalent positions of the coordinates (0.138, 0.018, 0.269), located approximately on the section passing through the 24*c* site and parallel to the (01$\bar{1}$) plane (Fig. 7a). We conducted a structure refinement based on the split-atom model assigning Mg to this peak position (96*h* model). The anisotropic refinement resulted in a non-positive-definite value for the anisotropic ADP of Mg. The refinement applying isotropic ADP (U_{iso}) only to Mg (96*h* Mg-isotropic refinement) converged successfully to R = 0.0151 and wR = 0.0084. These reliability indices are better than those of the 24*c* (Mg-isotropic) model (R = 0.0179, wR = 0.0093) and comparable to those of the refinement applying anisotropic ADPs to all atoms of the 24*c* model [24*c* anisotropic refinement; R = 0.0151, wR = 0.0084 (Table 1)]. The same results were obtained at all the investigated temperatures. Hamilton's significance tests on the *wR*-factor ratio (Hamilton 1965) indicate that at all the investigated temperatures, the 96*h* Mg-isotropic model is improved compared to the 24*c* Mg-isotropic model at the significance level $\alpha < 0.005$ (Table 5). Even when comparing the 96*h* Mg-isotropic model with the 24*c* anisotropic model, Hamilton's tests show that the former is better generally at $\alpha \leq 0.050$ level. Indeed, as shown in example at 96.7 K (Table 6), the 96*h* Mg-isotropic refinements converge to Mg positional parameters deviating significantly from the 24*c* site and to U_{iso}(Mg) significantly smaller than U_{eq}(Mg) in the 24*c* model (Table 2) as a consequence of the removal of the static disorder component. The temperature dependence of the U_{iso}(Mg) (Fig. 8) is comparable to that of the MSD_{ax1}(Mg), which has the smallest static disorder component and hence can approximately reflect the dynamic disorder of off-centered Mg, from the 24*c* anisotropic refinements (Fig. 6). To more directly confirm that the 96*h* position found here is a split-atom site of Mg, we compare the difference Fourier map at 96.7 K after the 24*c* Mg-isotropic refinement (Fig. 9a) with the one after the 96*h* Mg-isotropic refinement (Fig. 9b). The residual electron density peaks at this position are observed with a height of 0.85 eÅ^{-3} for the 24*c* Mg-isotropic model (Fig. 9a), whereas their peak heights in the 96*h* Mg-isotropic model (Fig. 9b) reduce dramatically to 0.13 eÅ^{-3}, a value even lower than a height of 0.14 eÅ^{-3} observed after the 24*c* anisotropic refinement (Fig. 7). Thus, the 96*h* model fits the electron density distributions better than the 24*c* model. Moreover, the projected components of the displacement vector between the 24*c* and the 96*h* sites are 0.019(14) Å to [100] (//axis 1), 0.038(6) Å to [01$\bar{1}$] (//axis 2), and 0.058(6) Å to [011] (//axis 3) at 96.7 K, agreeing within errors with $\sqrt{\langle u^2_{ax1}\rangle_{static}}$ [=0.033(2) Å], $\sqrt{\langle u^2_{ax2}\rangle_{static}}$ [=0.033(3) Å], and $\sqrt{\langle u^2_{ax3}\rangle_{static}}$ [=0.046(3) Å] of Mg (Table 4). Thus, the anisotropy of the Mg static disorder components is successfully explained by assuming only one split-atom site. From these results, we conclude that this 96*h* site is the split-atom site of Mg.

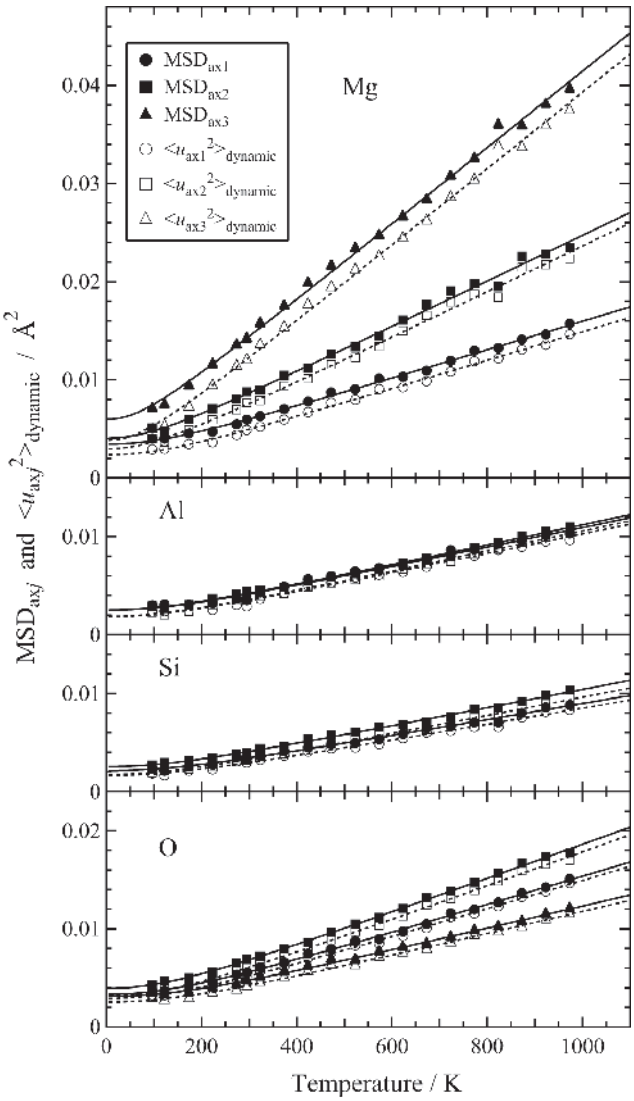

FIGURE 6. Temperature dependence of MSD_{axj} and its dynamic disorder component $\langle u^2_{axj}\rangle_{dynamic}$ in the direction of the axis *j*. The direction of the axis *j* for each atom is as in Table 4.

The 96*h* Mg-site has four equivalent positions distributed about 0.07 Å away from the nearest 24*c* position, as shown for example at 96.7 K. If Mg were dynamically hopping into adjacent Mg positions at a certain temperature, its ADP should increase steeply at this temperature. However, the U_{iso}(Mg) only increases monotonously with increasing temperature (Fig. 8).

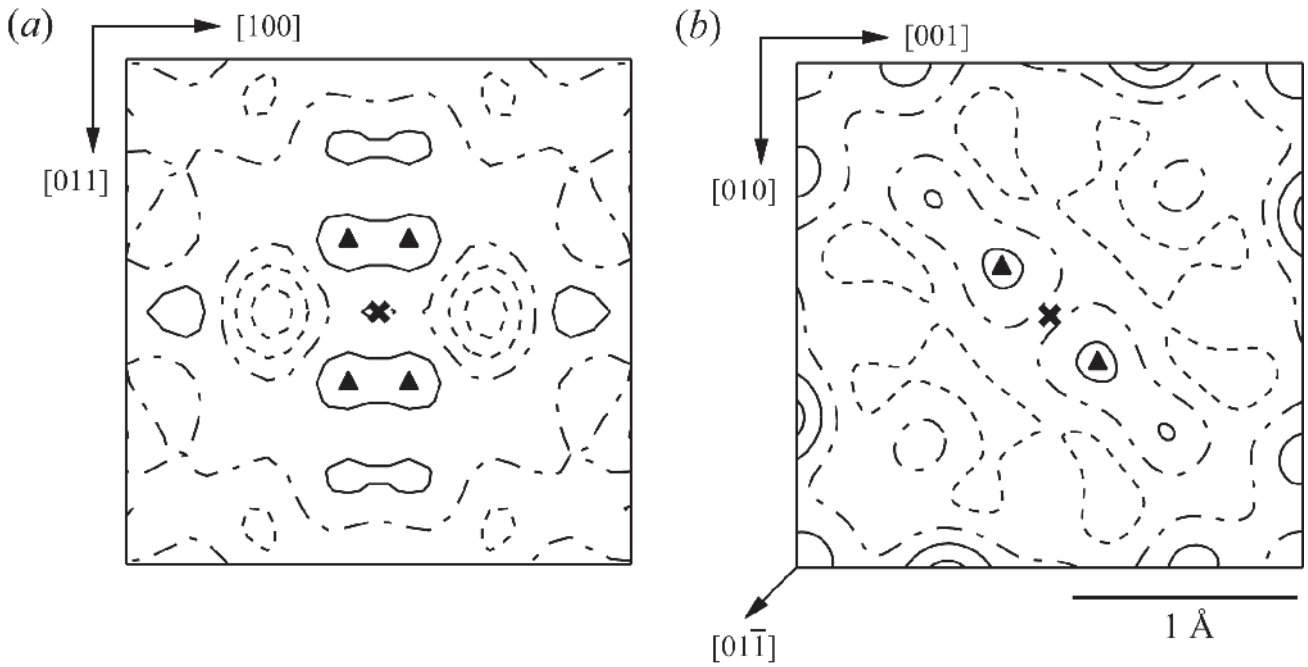

FIGURE 7. Difference Fourier maps at 96.7 K after the anisotropic refinement on the 24*c* model: (**a**) section passing through the 24*c* site and parallel to the (01$\bar{1}$) plane, (**b**) section passing through the 24*c* site and parallel to the (100) plane. The contour interval is 0.1 eÅ^{-3}. Positive contours are solid lines. Negative and zero contours are dashed lines and dashed-and-dotted lines, respectively. The 24*c* site at (0.125, 0, 0.25) is denoted with crosses (×). Solid triangles represent the residual electron density peaks due to the Mg static disorder.

TABLE 5. Results of Hamilton's significance tests

Model I: 24*c* model (only Mg isotropic) Model II: 96*h* model (only Mg isotropic)				Model I: 24*c* model (All atoms anisotropic) Model II: 96*h* model (only Mg isotropic)			Model I: 24*c* model (All atoms anisotropic) Model II: 24*c* model (All atoms anharmonic)		
T (K)	*R**	$R_{b,n-m,\alpha}$†	α(*R*)‡	*R**	$R_{b,n-m,\alpha}$†	α(*R*)‡	*R**	$R_{b,n-m,\alpha}$†	α(*R*)‡
96.7	1.105	1.022 (3, 302, 0.005)	<0.005	1.004	1.004 (1, 302, 0.100)	0.100	1.274	1.136 (44, 259, 0.005)	<0.005
122.3	1.092	1.022 (3, 305, 0.005)	<0.005	1.006	1.006 (1, 305, 0.050)	0.050	1.267	1.134 (44, 262, 0.005)	<0.005
173.7	1.185	1.022 (3, 301, 0.005)	<0.005	1.002	1.002 (1, 301, 0.250)	0.250	1.287	1.137 (44, 258, 0.005)	<0.005
223.3	1.393	1.021 (3, 307, 0.005)	<0.005	1.015	1.013 (1, 307, 0.005)	<0.005	1.291	1.133 (44, 264, 0.005)	<0.005
273.6	1.502	1.021 (3, 309, 0.005)	<0.005	1.001	1.001 (1, 309, 0.500)	0.500	1.285	1.132 (44, 266, 0.005)	<0.005
295	1.485	1.022 (3, 298, 0.005)	<0.005	1.010	1.008 (1, 298, 0.025)	0.010–0.025	1.295	1.138 (44, 255, 0.005)	<0.005
322.8	1.565	1.021 (3, 307, 0.005)	<0.005	1.013	1.013 (1, 307, 0.005)	0.005	1.313	1.133 (44, 264, 0.005)	<0.005
373.5	1.671	1.022 (3, 305, 0.005)	<0.005	1.012	1.011 (1, 305, 0.010)	0.005–0.010	1.291	1.134 (44, 262, 0.005)	<0.005
423.3	1.518	1.025 (3, 265, 0.005)	<0.005	1.001	1.001 (1, 265, 0.500)	0.500	1.295	1.159 (44, 222, 0.005)	<0.005
472.6	1.628	1.026 (3, 254, 0.005)	<0.005	1.003	1.003 (1, 254, 0.250)	0.250	1.445	1.167 (44, 211, 0.005)	<0.005
523.0	2.003	1.024 (3, 276, 0.005)	<0.005	1.000	1.001 (1, 276, 0.500)	>0.500	1.269	1.151 (44, 233, 0.005)	<0.005
572.9	1.905	1.024 (3, 273, 0.005)	<0.005	1.002	1.001 (1, 273, 0.500)	0.250–0.500	1.410	1.153 (44, 230, 0.005)	<0.005
622.9	2.092	1.025 (3, 269, 0.005)	<0.005	1.012	1.012 (1, 269, 0.010)	0.010	1.300	1.156 (44, 226, 0.005)	<0.005
672.9	2.095	1.026 (3, 252, 0.005)	<0.005	1.024	1.016 (1, 252, 0.005)	<0.005	1.296	1.169 (44, 209, 0.005)	<0.005
723.0	2.292	1.027 (3, 242, 0.005)	<0.005	1.025	1.017 (1, 242, 0.005)	<0.005	1.347	1.177 (44, 199, 0.005)	<0.005
773.1	2.231	1.028 (3, 234, 0.005)	<0.005	1.031	1.017 (1, 234, 0.005)	<0.005	1.413	1.184 (44, 191, 0.005)	<0.005
823.1	2.070	1.029 (3, 226, 0.005)	<0.005	1.008	1.008 (1, 226, 0.050)	0.050	1.287	1.192 (44, 183, 0.005)	<0.005
873.1	2.317	1.029 (3, 226, 0.005)	<0.005	1.012	1.011 (1, 226, 0.025)	0.010–0.025	1.296	1.192 (44, 183, 0.005)	<0.005
922.9	2.618	1.031 (3, 212, 0.005)	<0.005	1.016	1.016 (1, 212, 0.010)	0.010	1.394	1.208 (44, 169, 0.005)	<0.005
972.9	2.188	1.034 (3, 192, 0.005)	<0.005	1.043	1.021 (1, 192, 0.005)	<0.005	1.422	1.236 (44, 149, 0.005)	<0.005

* The ratio *wR*(I)/*wR*(II), where *wR*(I) and *wR*(II) are *wR* factors in Models I and II, respectively.
† The significance points of the *wR*-factor ratio at the significance level α, where *b* is the difference between number of parameters in Models II and I; $n - m$ is the difference between number of reflections and number of parameters in Model II. The values in parentheses represent (b, $n - m$, α).
‡ The significance levels of the present *wR*-factor ratios.

It is also unlikely that the Mg hopping already occurs at a low temperature < 96.7 K. Up to at least 972.9 K, the potential barriers among the adjacent Mg positions are thus considered to be larger than the kinetic energy $k_B T$.

Anharmonic structure refinements

Figure 10 shows the temperature dependence of the third- (γ_{ijk}) and fourth-rank (δ_{ijkl}) tensor coefficients obtained from the anharmonic refinements on the 24*c* model. Although the refined γ_{ijk} and δ_{ijkl} coefficients are rather small over the investigated temperature range, several of these show a significant deviation from zero with reliability levels of $>1\sigma$ at several temperature points. Typical examples are shown in Figure 10. With the exception of γ_{123} and γ_{223} of the O atom, only the fourth-rank tensor coefficients (δ_{ijkl}) were significant. Note that many of the higher-rank tensor coefficients selected for Figure 10 deviate significantly

TABLE 6. Structural parameters from the Mg-isotropic refinement on the 96*h* model at 96.7 K

Atom	Mg	Al	Si	O
Wyckoff position	96*h*	16*a*	24*d*	96*h*
Site occupancy	0.25	1	1	1
x	0.1267(12)	0	0.375	−0.03290(4)
y	0.0060(7)	0	0	0.05061(4)
z	0.2512(3)	0	0.25	0.15333(4)
U_{iso} or U_{eq} (Å^2)	0.0036(5)*	0.00292(1)†	0.00257(1)†	0.00383(3)†
$\beta_{11} \times 10^3$	–	0.440(2)	0.349(4)	0.552(4)
$\beta_{22} \times 10^3$	–	0.440	0.407(2)	0.652(4)
$\beta_{33} \times 10^3$	–	0.440	0.407	0.531(4)
$\beta_{12} \times 10^3$	–	0.004(3)	0	−0.072(3)
$\beta_{13} \times 10^3$	–	0.004	0	0.106(3)
$\beta_{23} \times 10^3$	–	0.004	0	0.028(3)

Notes: Reliability indices: $R = 0.0151$, $wR = 0.0084$.
* U_{iso}.
† U_{eq}.

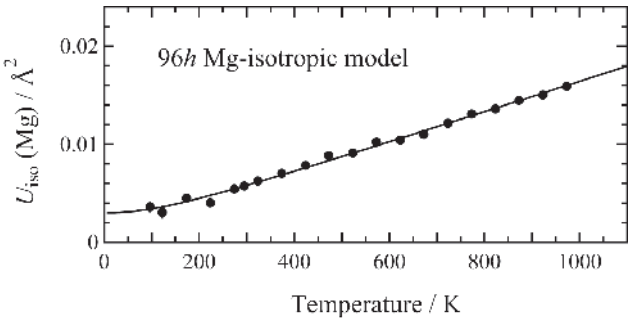

FIGURE 8. Temperature dependence of U_{iso}(Mg) from the Mg-isotropic refinements on the 96*h* model.

from zero even at a low temperature of 96.7 K [e.g., δ_{2222}(Mg), δ_{1111}(Al), δ_{1111}(Si), δ_{2222}(Si), γ_{123}(O), δ_{1111}(O), δ_{1122}(O), δ_{2222}(O), δ_{3333}(O)]. In connection with these deviations, the *R* and *wR* values were markedly improved over the investigated temperatures as a result of the introduction of higher-rank tensor coefficients (Table 1). Hamilton's significance tests indicate that all the present anharmonic refinements are significant at $\alpha < 0.005$ level (Table 5). Thus, it is certain that the probability density functions (PDFs) of all atoms are significantly deformed from ellipsoidal distributions even at a low temperature of 96.7 K. It is unreasonable that this deformation is attributed to the anharmonic contribution to atomic thermal vibrations, which should be in principle absent or minimal at such a low temperature in rigid crystals such as pyrope. In the difference Fourier map after the anharmonic refinement, the residual electron density peaks due to the Mg static disorder observed in Figure 7 almost entirely disappeared, as shown in example at 96.7 K (Fig. 11). Moreover, the ADPs of all atoms (Mg, Al, Si, O) include significant static disorder components (Table 4) as shown above and none of the non-zero higher-rank tensor coefficients shows systematic temperature dependence below at least 800 K (Fig. 10). From these considerations, we attribute the deformation of PDFs from ellipsoidal distributions observed even at low temperatures to the static disorder that occurs on all atoms. These results therefore contradict the idea that the anomalous coordination environment of Mg produces anharmonic thermal vibration even at room temperature, although the possibility of this anharmonic contribution has long been debated by many researchers (Pavese et al. 1995; Artioli et al. 1997; Winkler et al. 2000).

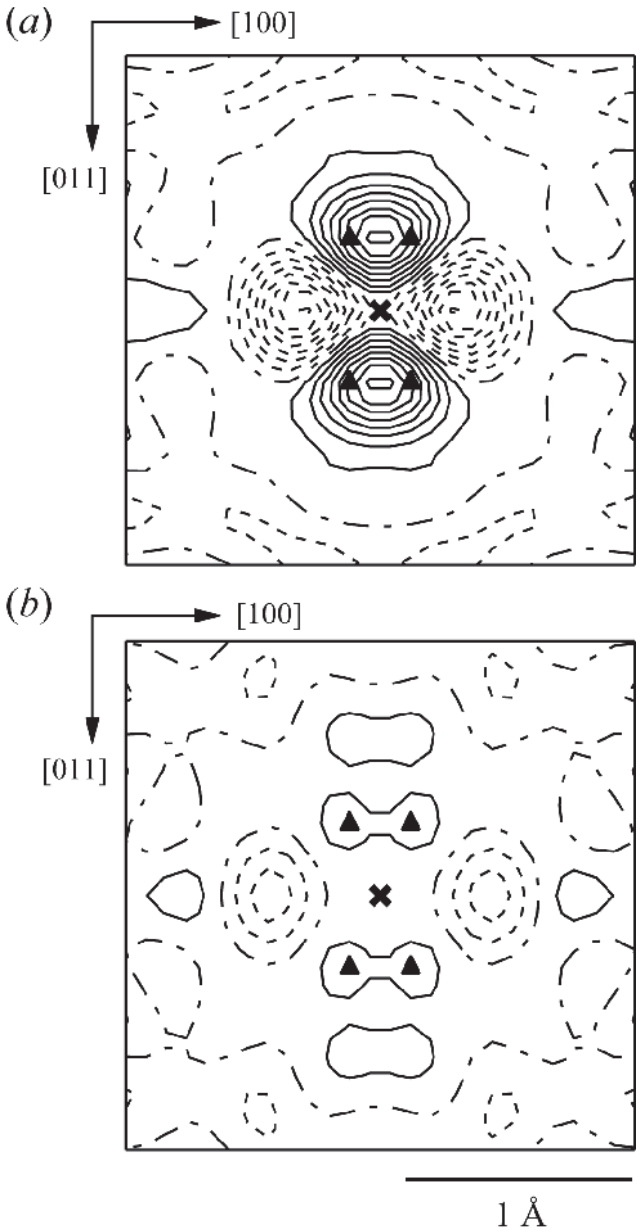

FIGURE 9. Difference Fourier maps at 96.7 K after the Mg-isotropic refinements, applying U_{iso} only to Mg, on (**a**) the 24*c* model and (**b**) the 96*h* model. A section passing through the 24*c* site and parallel to the (01$\bar{1}$) plane is shown here. The contour interval and the crosses (×) are as in Figure 7. Solid triangles indicate the peak positions observed in Figure 7.

On the other hand, many of the higher-rank tensor coefficients of Mg, Al, and O atoms selected for Figure 10 seem to be getting slightly but systematically larger in the deviation from zero with increasing temperature above about 800 K [e.g., δ_{2222}(Mg), δ_{2223}(Mg), δ_{1123}(Mg), δ_{2233}(Mg), δ_{1111}(Al), δ_{1122}(Al), γ_{123}(O), δ_{1122}(O)]. This behavior at high temperatures is indicative of an anharmonic contribution to atomic thermal vibrations. This is partially concordant with results of previous diffraction studies, which suggested an anharmonic contribution to thermal vibrations for Mg only (Pavese et al. 1995) or both Mg and O atoms (Artioli et al. 1997) at high temperatures above 700 K.

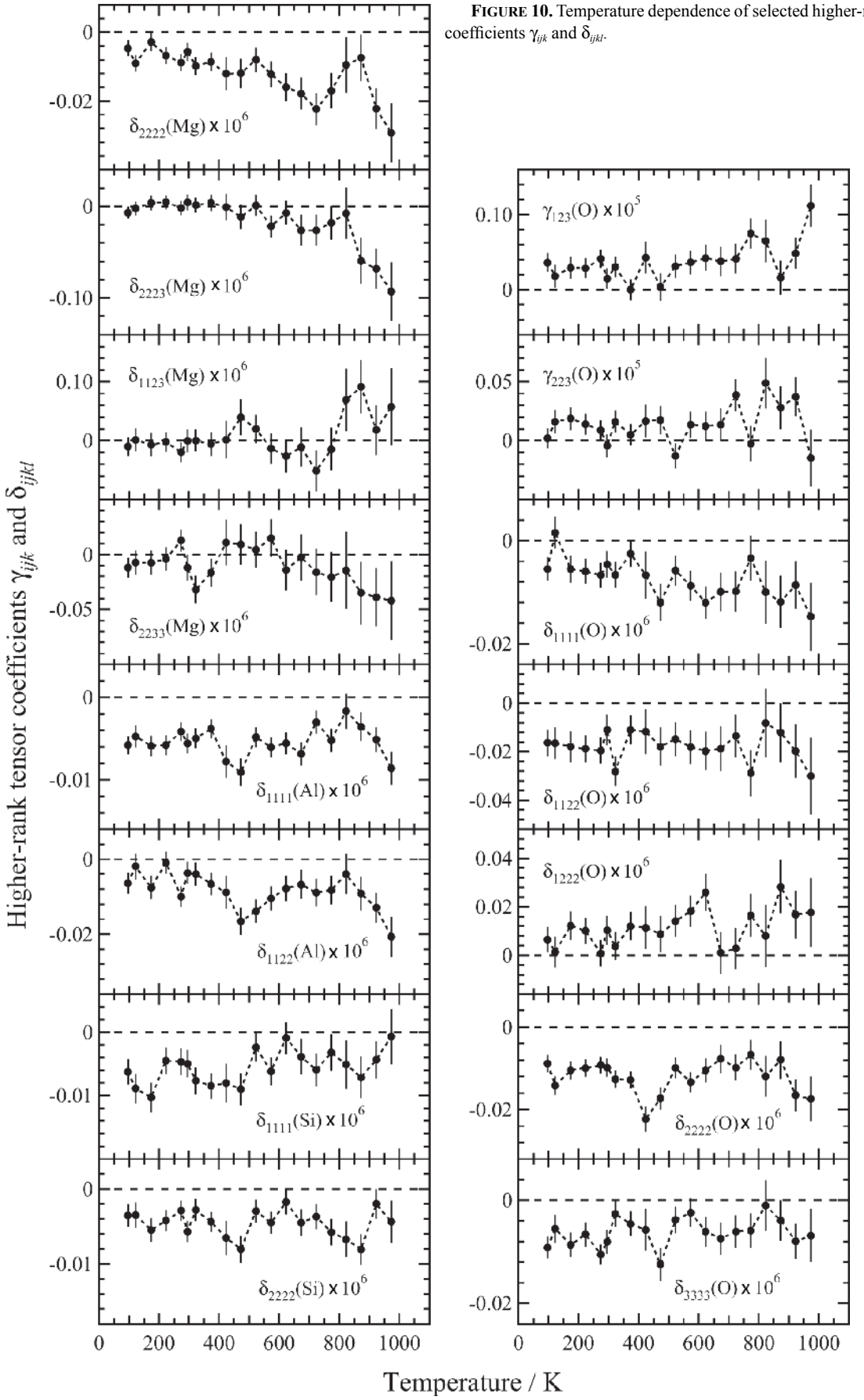

FIGURE 10. Temperature dependence of selected higher-rank tensor coefficients γ_{ijk} and δ_{ijkl}.

However, the present results suggest that Al atom also shows a significant anharmonic contribution at high temperatures above 800 K, as well as Mg and O atoms. In contrast, it is plausible that Si with rigid bonds does not display a significant anharmonicity of its thermal vibration above 800 K.

Concluding remarks

On the basis of the precise single-crystal X-ray diffraction structure analyses at low and high temperatures, we have disclosed the presence of a static disorder for Mg in pyrope, which has long been a controversial issue. We also propose the possibility of a static disorder for the Al, Si, and O sites. These findings lead to the conclusion that the static disorder of Mg is responsible for the peculiar behaviors that have been observed in pyrope, i.e., anomalously large ADP of Mg and anomalously high heat capacity at low temperature. In particular, the latter observation can be related to the static disorders of Al, Si, and O atoms as well. Such static disorders may also exist in the tetragonal garnet "majorite ($MgSiO_3$)," a major constituent in the transition zone of the Earth's mantle, because its dodecahedral Mg atoms have larger ADPs than that in pyrope (Angel et al. 1989).

In addition to the proper extraction of the static disorder components, the average of the Debye temperatures for each atom determined in the present study is comparable to the macroscopic values estimated from other properties, such as volumetric thermal expansion and acoustic wave velocity (e.g., Suzuki and Anderson 1983). This shows that the application of the Debye model to the temperature dependence of MSDs is a valid approach to examine the existence of static disorders and experimentally determine Debye temperatures if reliable ADPs are available. This approach has the advantages that microscopic Debye temperatures, determined individually for each atom in a crystal, can be obtained and their anisotropies can be determined from anisotropies of each MSD. Application of this approach to materials of the Earth's interior is promising for further understanding of physical and thermodynamic properties of the Earth's interior.

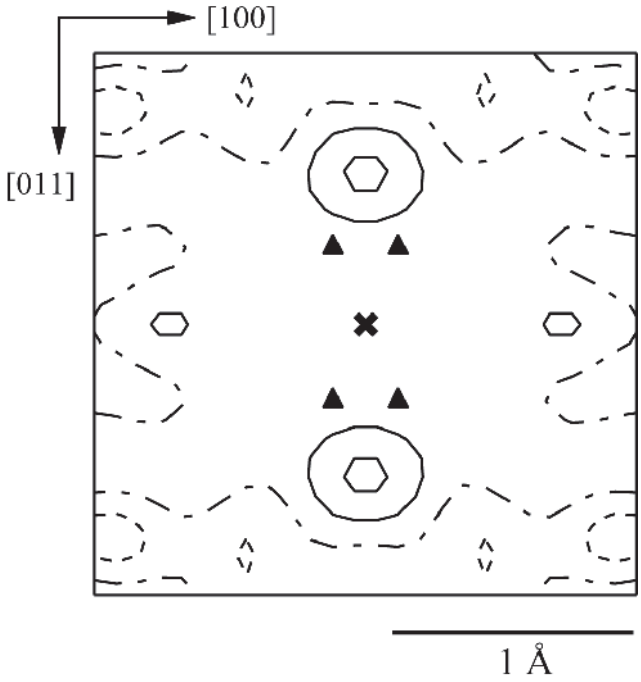

Figure 11. Difference Fourier map at 96.7 K after the anharmonic refinement on the 24*c* model. A section passing through the 24*c* site and parallel to the $(01\bar{1})$ plane is shown here. The contour interval and symbols are as in Figure 9.

Acknowledgments

We thank H. Okudera of Kanazawa University for critical reading of the paper and useful suggestions.

References cited

Armbruster, T. and Geiger, C.A. (1993) Andradite crystal chemistry, dynamic X-site disorder and structural strain in silicate garnets. European Journal of Mineralogy, 5, 59–71.

Angel, R.J., Finger, L.W., Hazen, R.M., Kanzaki, M., Weidner, D.J., Liebermann, R.C., and Veblen, D.R. (1989) Structure and twinning of single crystal $MgSiO_3$ garnet synthesized at 17 GPa and 1800 °C. American Mineralogist, 74, 509–512.

Armbruster, T., Geiger, C.A., and Lager, G.A. (1992) Single-crystal X-ray structure study of synthetic pyrope almandine garnets at 100 and 293 K. American Mineralogist, 77, 512–521.

Artioli, G., Pavese, A., Ståhl, K., and McMullan, R.K. (1997) Single-crystal neutron-diffraction study of pyrope in the temperature range 30-1173 K. The Canadian Mineralogist, 35, 1009–1019.

Becker, P.J. and Coppens, P. (1974a) Extinction within the limit of validity of the Darwin transfer equations. I. General formalisms for primary and secondary extinction and their application to spherical crystals. Acta Crystallographica, A30, 129–147.

Becker, P.J. and Coppens, P. (1974b) Extinction within the limit of validity of the Darwin transfer equations. II. Refinement of extinction in spherical crystals of SrF_2 and LiF. Acta Crystallographica, A30, 148–153.

Brown, G.E. and Prewitt, C.T. (1973) High-temperature crystal chemistry of hortonolite. American Mineralogist, 58, 577–587.

Christensen, M., Lock, N., Overgaard, J., and Iversen, B.B. (2006) Crystal structure of thermoelectric n- and p-type $Ba_8Ga_{16}Ge_{30}$ studied by single crystal, multi-temperature, neutron diffraction, conventional X-ray diffraction and resonant synchrotron X-ray diffraction. Journal of American Chemical Society, 128, 15657–15665.

Cressey, G. (1981) Entropies and enthalpies of aluminosilicate garnets. Contributions to Mineralogy and Petrology, 76, 413–419.

Etschmann, B., Streltsov, V., Ishizawa, N., and Maslen, E.N. (2001) Synchrotron X-ray study of $Er_3Al_5O_{12}$ and $Yb_3Al_5O_{12}$ garnets. Acta Crystallographica, B57, 136–141.

Euler, F. and Bruce, J.A. (1965) Oxygen coordinates of compounds with garnet structure. Acta Crystallographica, 19, 971–978.

Fei, Y. (1995) Thermal expansion. In T.J. Ahrens, Ed., Mineral Physics and Crystallography—A Handbook of Physical Constants, p. 29–44. American Geophysical Union, Reference Shelf 2, Washington, D.C.

Geiger, C.A. and Armbruster, T. (1997) $Mn_3Al_2Si_3O_{12}$ spessartine and $Ca_3Al_2Si_3O_{12}$ grossular garnet: Structural dynamic and thermodynamic properties. American Mineralogist, 82, 740–747.

Geiger, C.A., Armbruster, T., Lager, G.A., Jiang, K., Lottermoser, W., and Amthauer, G. (1992a) A combined temperature dependent ^{57}Fe Mössbauer and single crystal X-ray diffraction study of synthetic almandine: Evidence for the Gol'danskii-Karyagin effect. Physics and Chemistry of Minerals, 19, 121–126.

Geiger, C.A., Merwin, L., and Sebald, A. (1992b) Structural investigation of pyrope garnet using temperature-dependent FTIR and ^{29}Si and ^{27}Al MAS NMR spectroscopy. American Mineralogist, 77, 713–717.

Gibbs, G.V. and Smith, J.V. (1965) Refinement of the crystal structure of synthetic pyrope. American Mineralogist, 50, 2023–2039.

Gramaccioli, C.M., Pilati, T., and Demartin, F. (2002) Atomic displacement parameters for spessartine $Mn_3Al_2Si_3O_{12}$ and their lattice-dynamical interpretation. Acta Crystallographica, B58, 965–969.

Hamilton, W.C. (1965) Significance tests on the crystallographic R factor. Acta Crystallographica, 18, 502–510.

Haselton, H.T. and Westrum, E.F. (1980) Low temperature heat capacities of synthetic pyrope, grossular and $pyrope_{60}grossular_{40}$. Geochimica et Cosmochimica Acta, 44, 701–709.

Hazen, R.M. and Finger, L.W. (1982) Comparative Crystal Chemistry, 231 p. Wiley, New York.

Hofmeister, A.M. and Chopelas, A. (1991) Thermodynamic properties of pyrope and grossular from vibrational spectroscopy. American Mineralogist, 76, 880–891.

Kieffer, S.W. (1980) Thermodynamics and lattice vibrations of minerals: 4. Application to chain and sheet silicates and orthosilicates. Reviews of Geophysics and Space Physics, 18, 862–886.

Kolesov, B.A. and Geiger, C.A. (1998) Raman spectra of silicate garnets. Physics and Chemistry of Minerals, 25, 142–151.

Levy, D. and Barbier, J. (1999) Normal and inverse garnets: $Ca_3Fe_2Ge_3O_{12}$, $Ca_3Y_2Ge_3O_{12}$ and $Mg_3Y_2Ge_3O_{12}$. Acta Crystallographica, C55, 1611–1614.

Lobanov, N.N., Butman, L.A., and Tsirel'son, V.G. (1989) Precision X-ray diffraction study of the garnets $Na_3Sc_2V_3O_{12}$ and $Na_{0.90}Ca_{2.38}Mn_{1.72}V_3O_{12}$. Journal of Structural Chemistry, 30, 96–104.

Meagher, E.P. (1975) The crystal structures of pyrope and grossularite at elevated temperatures. American Mineralogist, 60, 218–228.

Nakatsuka, A., Yoshiasa, A., and Takeno, S. (1995) Site preference of cations and structural variation in $Y_3Fe_{5-x}Ga_xO_{12}$ ($0 \le x \le 5$) solid solution with garnet structure. Acta Crystallographica, B51, 737–745.

Nakatsuka, A., Yoshiasa, A., and Yamanaka, T. (1999a) Cation distribution and crystal chemistry $Y_3Al_{5-x}Ga_xO_{12}$ ($0 \le x \le 5$) garnet solid solutions. Acta Crystallographica, B55, 266–272.

Nakatsuka, A., Yoshiasa, A., Yamanaka, T., Ohtaka, O., Katsura, T., and Ito, E. (1999b) Symmetry change of majorite solid-solution in the system $Mg_3Al_2Si_3O_{12}$-$MgSiO_3$. American Mineralogist, 84, 1135–1143.

Nakatsuka, A., Ikuta, Y., Yoshiasa, A., and Iishi, K. (2003) Vanadate garnet, $Ca_2NaMg_2V_3O_{12}$. Acta Crystallographica, C59, i133–i135.

Nakatsuka, A., Ikuta, Y., Yoshiasa, A., and Iishi, K. (2004) Single crystal X-ray diffraction study of the vanadate garnet $Ca_2NaZn_2V_3O_{12}$. Materials Research Bulletin, 39, 949–956.

Nakatsuka, A., Chaya, H., and Yoshiasa, A. (2005) Crystal structure of single-crystal $CaGeO_3$ tetragonal garnet synthesized at 3 GPa and 1000 °C. American Mineralogist, 90, 755–757.

Novak, G.A. and Gibbs, G.V. (1971) The crystal chemistry of silicate garnets. American Mineralogist, 56, 791–825.

Pauling, L. (1929) The principles determining the structure of complex ionic crystals. Journal of the American Chemical Society, 51, 1010–1026.

Pavese, A., Artioli, G., and Prencipe, M. (1995) X-ray single-crystal diffraction study of pyrope in the temperature range 30–973 K. American Mineralogist, 80, 457–464.

Pilati, T., Demartin, F., and Gramaccioli, C.M. (1996) Atomic displacement parameters for garnets: A lattice-dynamical evaluation. Acta Crystallographica, B52, 239–250.

Rodehorst, U., Geiger, C.A., and Armbruster, T. (2002) The crystal structures of grossular and spessartine between 100 and 600 K and the crystal chemistry of grossular-spessartine solid solutions. American Mineralogist, 87, 542–549.

Sasaki, S. (1987) RADY. A Fortran program for the least-squares refinement of crystal structures. National Laboratory for High Energy Physics, Japan.

Sawada, H. (1993) The crystal structure of garnets (I): The residual electron density distribution in pyrope. Zeitschrift für Kristallographie, 203, 41–48.

Sinogeikin, S.V. and Bass, J.D. (2002) Elasticity of pyrope and majorite-pyrope solid solutions to high temperatures. Earth and Planetary Science Letters, 203, 549–555.

Smyth, J.R. and Hazen, R.M. (1973) The crystal structures of forsterite and hortonolite at several temperatures up to 900 °C. American Mineralogist, 58, 588–593.

Suzuki, I. and Anderson, O.L. (1983) Elasticity and thermal expansion of a natural garnet up to 1000 K. Journal of Physics of the Earth, 31, 125–138.

Suzuki, I., Okajima, S., and Seya, K. (1979) Thermal expansion of single-crystal manganosite. Journal of Physics of the Earth, 27, 63–69.

Tokonami, M. (1965) Atomic scattering factor for O^{2-}. Acta Crystallographica, 19, 486.

Tsirlin, A.A., Dikarev, E.V., Velikodny, Y.A., Shpanchenko, R.V., and Antipov, E.V. (2007) $Pb_{2.63}Cd_2V_3O_{12}$, a cation-deficient garnet-type vanadate. Acta Crystallographica, C63, i40–i42.

Willis, B.T.M. and Pryor, A.W. (1975) Thermal Vibrations in Crystallography. Cambridge University Press, U.K.

Wilson, A.J.C., Ed. (1992) International Tables for Crystallography, vol. C. Kluwer, Dordrecht.

Winkler, B., Dove, M.T., and Leslie, M. (1991) Static lattice energy minimization and lattice dynamics calculations on aluminosilicate minerals. American Mineralogist, 76, 313–331.

Winkler, B., Milman, V., Akhmatskaya, E.V., and Nobes, R.H. (2000) Bonding and dynamics of Mg in pyrope: A theoretical investigation. American Mineralogist, 85, 608–612.

Wood, I.G., Knight, K.S., Price, G.D., and Stuart, J.A. (2002) Thermal expansion and atomic displacement parameters of cubic $KMgF_3$ perovskite determined by high-resolution neutron powder diffraction. Journal of Applied Crystallography, 35, 291–295.

Yoshiasa, A., Nakatsuka, A., and Ohkawa, M. (1997) EXAFS study on the short-range correlation of vibrational motion in the $Y_3Fe_{5-x}Ga_xO_{12}$ garnet solid solution. Mineralogical Journal, 19, 21–32.

Zemann, J. (1962) Zur Kristallchemie der Granate. Beiträge zur Mineralogie und Petrologie, 8, 180–188.

MANUSCRIPT RECEIVED OCTOBER 7, 2010
MANUSCRIPT ACCEPTED MAY 16, 2011
MANUSCRIPT HANDLED BY ALEXANDRA FRIEDRICH